

**This manuscript has been accepted for publication in *Geochimica et Cosmochimica Acta*
(<https://doi.org/10.1016/j.gca.2024.06.025>)**

Degree of sector zoning in clinopyroxene records dynamic magma recharge and ascent

Alice MacDonald^{1*}, Teresa Ubide¹, Silvio Mollo^{2,3}

¹School of the Environment, The University of Queensland, St Lucia, Queensland, 4072, Australia

²Department of Earth Sciences, Sapienza – University of Rome, P. le Aldo Moro 5, 00185 Roma, Italy

³Istituto Nazionale di Geofisica e Vulcanologia – INGV, Via di Vigna Murata 605, 00143 Roma, Italy

*Corresponding author: alice.macdonald@uq.edu.au

1 **Abstract**

2 The development of sector zoning in clinopyroxene is attributed to the influence of
3 crystallisation kinetics imposed by magma undercooling (ΔT) and may reflect variations in
4 magma cooling histories. Yet, the degree of compositional variations between sectors has not
5 been explored as a potential recorder of crystallisation dynamics. Here, we investigate the
6 distribution of major, minor, and trace elements between hourglass $\{-1\ 1\ 1\}$ and prism $\{h\ k\ 0\}$
7 sectors in clinopyroxene with distinct pre-eruptive histories at Mt. Etna, Italy. We analyse
8 sector-zoned clinopyroxene crystals ranging in size from sub-mm to cm (i.e.,
9 microphenocrysts, phenocrysts, and megacrysts), from eruptions fed by the central conduits
10 of the volcano (1669 and 2002-03 flank eruptions) and eruptions fed by eccentric dykes
11 which bypass the central conduits, tapping deeper magma storage regions (1974 and 2002-03
12 flank eruptions). We focus on Cr-rich mantle zones, which crystallised upon eruption
13 triggering mafic rejuvenation and are ubiquitous across our sample set. With decreasing
14 crystal size (i.e., increasing ΔT), tetrahedral aluminium is more strongly partitioned between
15 prism and hourglass sectors. This promotes the uptake of rare earth elements (REE) and high
16 field strength elements (HFSE) into prism relative to hourglass sectors. Combining relative
17 degrees of sector enrichment with ΔT estimates, we propose magma recharge, mush
18 remobilisation and the onset of magma ascent imposed slightly higher ΔT in 1974 than in
19 2002-03 eruptions at Mt. Etna. Enhanced ΔT in 1974 could be related to vigorous mixing and
20 rapid transport of magma with limited storage, resulting in crystals of smaller sizes. Crystal
21 size populations vary across eruptions, but crystals within a given population (e.g.,
22 phenocrysts) return similar calculated ΔT and REE + HFSE sector enrichments, implying
23 connectivity between magmatic environments in the mush system. We show that the
24 magnitude of sector zoning in clinopyroxene can be employed to explore subtle differences in
25 pre-eruptive dynamics in volcanic systems. As an example, we explore sector enrichment in

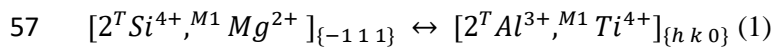
26 clinopyroxene phenocrysts from the 2021 eruption at La Palma (Canary Islands) and
27 megacrysts from Roman era activity at Stromboli (Italy). Results highlight the role of
28 dynamic mixing and mush remobilisation before eruption in mafic alkaline settings and
29 suggest changes in magma composition across alkaline systems influence clinopyroxene
30 chemistry but do not influence sector enrichment.

31 **Keywords:** Clinopyroxene, Sector zoning, LA-ICP-MS Mapping, Mt. Etna, Undercooling

32 **1. Introduction**

33 Textural and compositional variations in igneous minerals provide a critical means of
34 understanding magmatic histories in volcanic plumbing systems. The sensitivity of mineral
35 zoning to changes in the physical and chemical state of a magma can be utilised to decipher
36 magmatic processes occurring in the lead up to volcanic eruptions (Putirka, 2008; Streck,
37 2008; Ubide and Kamber, 2018). Clinopyroxene is common in mafic to intermediate magmas
38 and can be used to unravel magmatic histories in a range of volcanic settings (e.g., Neave et
39 al., 2014; Mollo et al., 2015; Giacomoni et al., 2016; Di Stefano et al., 2020; Pontesilli et al.,
40 2021; Ruth and Costa, 2021; Tapu et al., 2022). Due to its slow lattice diffusion compared to
41 other volcanic minerals, such as olivine (Van Orman et al., 2001; Müller et al., 2013; Costa et
42 al., 2020), sensitivity to changes in crystallisation conditions (Streck, 2008; Neave and
43 Putirka, 2017; Mollo et al., 2018), and stability over a broad range of conditions (Armienti et
44 al., 2007; Putirka, 2008; Mollo et al., 2015; Perinelli et al., 2016), clinopyroxene is able to
45 store a protracted record of pre-eruptive processes as compositional zoning patterns.
46 However, records of magmatic processes locked within clinopyroxene crystals are not always
47 easily interpreted. In addition to concentric zoning associated with temporal changes in
48 magma temperature, depth and composition, clinopyroxene crystals growing from a single
49 melt may also be sector-zoned, with distinct chemical compositions growing along different
50 crystallographic orientations. Sector-zoned crystals consist of ‘hourglass’ sectors $\{-111\}$,

51 growing rapidly along the c -axis, and coeval ‘prism’ sectors $\{h k 0\}$, growing relatively
 52 slowly perpendicular to the c -axis, with a distinct composition (Leung, 1974; Dowty, 1976;
 53 Ubide et al., 2019a). Typically, hourglass sectors are enriched in Si compared to prism
 54 sectors, which incorporate higher amounts of Al substituting for Si in the tetrahedral site, and
 55 highly charged cations such as Ti balancing the charge deficit in the M1 site (Ubide et al.,
 56 2019a; Di Fiore et al., 2021).



58 Charge imbalance due to $Si \leftrightarrow Al$ substitution causes an increased uptake of highly charged
 59 trace cations, such as rare earth elements (REE) and high field strength elements (HFSE) into
 60 prism sectors, resulting in compositional contrasts between sectors. Therefore, Eq. (1) can be
 61 re-evaluated in terms of hypothetical clinopyroxene components for Ts ($Ts = CaAl_2SiO_6 +$
 62 $CaFeSiAlO_6$) and Di ($CaMgSi_2O_6$), expressing the major cation distributions in the lattice
 63 site. As a result, $REETs$ and $HFSETs$ are enriched in $\{h k 0\}$ relative to $\{-1\ 1\ 1\}$ (MacDonald
 64 et al., 2022).

65 The occurrence of sector zoning can be attributed to a combination of the architecture of
 66 crystal faces, the relative diffusion of cation species in the melt, and the relative growth rates
 67 of clinopyroxene along different crystallographic axes (Nakamura, 1973; Downes, 1974;
 68 Leung, 1974; Dowty, 1976; Shimizu, 1981; Mollo et al., 2023), driven by magma
 69 undercooling ($\Delta T = T_{liquidus} - T_{crystallisation}$; Kirkpatrick 1981). Experimentally, the presence of
 70 sector zoning in clinopyroxene in mafic alkaline systems has been observed at low ΔT ,
 71 associated with interface growth kinetics at near-equilibrium conditions ($\Delta T < 45\ ^\circ C$; Kouchi
 72 et al., 1981; Masotta et al., 2020). Undercooling exerts a significant influence on crystal
 73 morphology, size and chemistry (Dowty, 1980; Kouchi et al., 1983; Shea and Hammer, 2013;
 74 Mollo and Hammer, 2017; MacDonald et al., 2022), and can be induced in a magma by

75 cooling, mixing, or exsolution of H₂O, which may be driven by decompression (e.g., Ubide et
76 al., 2021). The presence and degree of sector zoning can also indicate magma ΔT (Kouchi et
77 al., 1983; Ubide et al., 2019a; Mollo et al., 2023), and larger compositional contrasts between
78 sectors have been observed in plagioclase crystals at increasing cooling rates (Lofgren, 1980;
79 Smith and Lofgren, 1983). However, the relationship between ΔT and the extent of elemental
80 partitioning between sectors remains underexplored. In clinopyroxene, a better understanding
81 of the impact of magma ΔT on zoning may provide new insights into processes of cooling
82 and degassing associated with distinct magmatic pathways and ascent in mafic to
83 intermediate settings (Mollo et al., 2013, 2023; Ubide et al., 2019a; Masotta et al., 2020;
84 MacDonald et al., 2022).

85 Here, we investigate the compositional contrasts between sectors in clinopyroxene
86 microphenocrysts, phenocrysts and megacrysts from eruptions fed by distinct pathways at
87 Mt. Etna, Italy, to investigate the effects of both crystal size and magmatic pathway on the
88 development of sector zoning. Mt. Etna is one of the most active, and well monitored,
89 volcanoes in Europe. Eruptions can be classified as either ‘central conduit’, where magma
90 travels through the complex central conduit system, or less commonly ‘eccentric’, where
91 magma bypasses the central conduit and travels rapidly to the surface, undergoing minimal
92 degassing (Clocchiatti et al., 2004; Métrich et al., 2004; Corsaro et al., 2009; Fig. 1).
93 Clinopyroxene is common in products of both eruption types and is stable across most of the
94 vertically extensive plumbing system, as outlined by thermodynamic modelling and
95 thermobarometry (Armienti et al., 2007; Armienti et al., 2013). Concentric zones enriched in
96 Cr and Mg and depleted in REE and HFSE are common close to clinopyroxene rims and
97 testify to the input of slightly more mafic magma into the main storage region (~ 10 km
98 depth) at Mt. Etna, which is commonly interpreted as an eruption trigger (Ubide and Kamber,
99 2018). Following the definitions of Kent et al., (2023), we refer to these events as mafic

100 rejuvenation (i.e., the input of mafic magma into a predominantly mafic system). Here, we
101 focus on these zones, which we refer to as Cr-rich mantles to differentiate them from the
102 outermost, Cr-poor rims which are interpreted as recorders of final crystallisation upon ascent
103 and eruption (Ubide and Kamber, 2018). We apply high resolution laser ablation mass
104 spectrometry mapping to explore the degree of partitioning between sectors in Cr-rich
105 mantles across crystal sizes and eruption types and assess the relationship with between
106 sector partitioning and inferred ΔT . Our results provide insights into the roles of magmatic
107 pathways and crystal sizes on the development of sector zoning in clinopyroxene from a
108 range of alkaline magma compositions.

109

110 **2. Materials and Methods**

111 **2.1. Samples**

112 This study uses a variety of sector-zoned clinopyroxene crystals from the 1669, 1974 and
113 2002-03 eruptions at Mt. Etna (see Fig. S1 for photomicrographs). We use the largest crystal
114 size population from each eruption as best representative of magma storage; 1) megacrysts
115 from the 1669 eruption, 2) phenocrysts from the 2002-03 central conduit and eccentric
116 eruptions, and 3) microphenocrysts from the 1974 eruption. Groundmass compositions from
117 all eruptions studied here are trachybasalts (Fig. S2), with similar concentrations of SiO₂ (~
118 48 wt. %) and Al₂O₃ concentrations varying from 16.4 wt. % (1974 eccentric) to 19.1 wt. %
119 (1669). The 1669 eruption was fed by the central conduits, generating a monogenetic cone on
120 the southern flank of the volcano (Monti Rossi) and an extensive lava field that reached part
121 of the city of Catania (Corsaro et al., 1996; Mulas et al., 2016; Kahl et al., 2017; Magee et al.,
122 2020), erupting lavas with plagioclase, clinopyroxene, and olivine phenocrysts (Corsaro et
123 al., 1996; Kahl et al., 2017; Fig. S2a). We use clinopyroxene megacrysts (> 5000 μm length)
124 from weathered scoria fragments collected from the crater rim of the Monti Rossi scoria

125 cone, previously described by Magee et al. (2020). This former study focused on core to rim
126 oscillatory zoning using megacrysts mounted perpendicular to the *c*-axis to minimise the
127 effect of sector-zoning. Here, we use clinopyroxene megacrysts from the same sample set,
128 but mounted parallel to the *c*-axis to effectively investigate sector zoning (Fig. S1a).
129 We also use clinopyroxene phenocrysts (1000 – 5000 μm length, Fig. S1 c-d; note we adopt
130 the term ‘phenocryst’ strictly to refer to crystal size, not the origin of these crystals.) from
131 samples erupted during the 2002-03 fissure eruption, with simultaneous outpourings of
132 trachybasaltic lava at the north-east rift (central conduit) and south rift (eccentric) of the
133 volcano (Clocchiatti et al., 2004; Andronico et al., 2005). We use samples previously
134 characterised in Magee et al. (2021), who focused on elemental and isotope variations in
135 matrix geochemistry on timescales of days to months. Although groundmass compositions
136 from both eccentric and central conduit eruptions classify as trachybasalts (Fig. S2a), their
137 bulk mineralogy differs. Lavas from the central conduit eruptions have abundant phenocrysts,
138 including plagioclase, clinopyroxene and olivine with titanomagnetite inclusions. In contrast,
139 plagioclase is absent as a phenocryst phase in eccentric lavas (Kahl et al., 2015; Magee et al.,
140 2021).

141 We integrate results from the 1669 megacrysts and 2002-03 phenocrysts with
142 microphenocrysts erupted in the 1974 eccentric eruption reported in Ubide et al. (2019a). The
143 1974 eccentric eruption generated two scoria cones and associated trachybasaltic lava flows
144 on the western flank of the volcano, concomitant with minor summit activity (Corsaro et al.,
145 2009). Lavas contain clinopyroxene and olivine microphenocrysts, with plagioclase restricted
146 to the groundmass. We test if decreasing crystal sizes from megacrysts to microphenocrysts
147 across the studied sample suite, inferred to reflect increasing nucleation rates and magma
148 undercooling, impacts the degree of compositional enrichment of prism sectors relative to
149 hourglass sectors in clinopyroxene.

150 **2.2 Analytical methods**

151 Major element compositions of clinopyroxene megacrysts from the 1669 eruption were
152 determined by electron probe microanalysis (EPMA) on carbon coated resin mounts using a
153 JEOL JXA 8530F Hyperprobe equipped with five wavelength dispersive spectrometers at the
154 Central Analytical Research Facility (CARF) at the Queensland University of Technology,
155 Australia. Analyses used an accelerating voltage of 15 kV, a beam current of 30 nA and a
156 beam size of 3 μm . Line transects were conducted across hourglass and prism sectors, and
157 across concentric zones within sectors, with variable spacings between points. In addition,
158 manually selected points targeting hourglass and prism sectors were also used, resulting in a
159 total of 75 analytical points for clinopyroxene mantles. Counting times for elements were 20
160 s on and off peak for all elements; except Cr and Ni, which were counted for 30 s on and off
161 peak, and Na which was counted for 10s on peak and 10s off peak. The instrument was
162 calibrated using: NBS K411 glass (Si-TAP, Mg-TAPH), rutile (Ti-LIFH), plagioclase (Al-
163 TAP), Cr oxide (Cr-LiFL), hematite (Fe – LIFH), Rhodonite (Mn – LIFH), Ni₉₀Fe₁₀ alloy
164 metal (Ni – LiFL), wollastonite (Ca – PETJ) and albite (Na – TAPH) standards. To monitor
165 data quality, we routinely analysed an in-house clinopyroxene standard (Table S1). Accuracy
166 was typically better than 4%, except for Ni which was typically below the detection limit.
167 Precision was typically better than 2% for major elements >1 wt.% abundance, and better
168 than 5% for minor elements <1 wt.% abundance. Precision based on EPMA-outputted
169 uncertainties yield similar results, with precision typically better than 1% for elements >1 wt.
170 % abundance, and better than 6% for elements <1 wt.% (Table S3). Results were filtered
171 using mineral stoichiometry and analytical totals. Major element compositions for the 2002-
172 03 eccentric phenocrysts and 1974 microphenocrysts are from Ubide et al. (2019a).

173 We used laser ablation inductively coupled mass spectrometry (LA-ICP-MS) to produce trace
174 element maps of clinopyroxene crystals from the 1669 and 2002-03 (central conduit and

175 eccentric) eruptions, following the method of Ubide et al., (2015). Mapping areas for the
176 1669 megacrysts were selected using EPMA imaging and analyses, including both hourglass
177 and prism sectors. Sector-zoned crystals from the 2002-03 eruptions were selected using thin
178 section microscopy. Analyses were conducted at The University of Queensland Centre for
179 Geoanalytical Mass Spectrometry, Radiogenic Isotope Facility (UQ RIF-lab), using an ASI
180 RESOLUTION 193 nm excimer UV ArF laser ablation system with a dual-volume Laurin
181 Technic ablation cell and GeoStar Norris software, in conjunction with a Thermo iCap RQ
182 quadrupole mass spectrometer and Qtegra software. Ablation was conducted under ultrapure
183 He conditions, with trace N₂ and Ar make up gas to aid in efficient transport and ionisation of
184 ablated material. The instrument was calibrated using NIST612 glass reference material prior
185 to analysis. A range of square spot sizes were used, depending on the crystal size and target
186 area. For the 1669 megacrysts, we used 30 × 30 μm, with a scan speed of 30 μm/s, a
187 repetition rate of 10 Hz and a fluence of 3 J/cm², with a path separation of 1 μm. For the
188 2002-03 eccentric and central conduit phenocrysts, we used smaller square spot sizes of 12 ×
189 12 μm or 20 × 20 μm, corresponding to scan speeds of 12 μm/s or 20 μm/s, respectively.
190 Each crystal was analysed twice with different sets of analytes, following Ubide et al.
191 (2019a). The first analyte menu included ⁷Li, ²³Na, ²⁷Al, ⁴³Ca, ⁴⁵Sc, ⁴⁹Ti, ⁵¹V, ⁵²Cr, ⁶⁰Ni, ⁸⁸Sr,
192 ⁹⁰Zr, ⁹³Nb, ¹⁷⁸Hf and ¹⁸¹Ta, with a total sweep time of 147 ms. The second analyte menu
193 included ⁴³Ca, ⁸⁹Y, ¹³⁹La, ¹⁴⁰Ce, ¹⁴¹Pr, ¹⁴⁶Nd, ¹⁴⁷Sm, ¹⁵³Eu, ¹⁵⁷Gd, ¹⁵⁹Tb, ¹⁶³Dy, ¹⁶⁵Ho, ¹⁶⁶Er,
194 ¹⁶⁹Tm, ¹⁷²Yb and ¹⁷⁵Lu, with a sweep time of 195 ms. Additional trace element maps of 2002-
195 03 clinopyroxene phenocrysts were produced using a QuadLock (©Norris Scientific) add-on
196 for the LA ICP-MS system, and a Fast Funnel (©Norris Scientific) adaptor add-on for the
197 laser ablation cell. The ablation cell was connected to the ICP-MS using a small diameter
198 tube (1 mm inner diameter), with a short length (~60 cm) which allowed for faster washout
199 times. For maps produced using this technique, we used a square spot size of 12 × 12 μm, a

200 scan speed of 40 $\mu\text{m/s}$, a repetition rate of 74 Hz and a fluence of 3 J/cm^2 . We also produced
201 maps using a square spot size of $20 \times 20 \mu\text{m}$ and a scan speed of 60 $\mu\text{m/s}$ for larger crystals.
202 We used a single analyte menu, combining the menus outlined previously, with a total dwell
203 time of 165 ms.

204 Trace element maps were produced using Iolite v4 (Paton et al., 2011) in quantitative mode.
205 We used NIST612 glass reference material as the calibration standard for all analytes, except
206 Ti and Cr for which we used BHVO-2G glass reference material. Calcium concentrations
207 measured by EPMA are typically homogenous in our crystals and therefore used as the
208 internal standard: 21.7 wt. % CaO for 1669 megacrysts and 22.2 wt. % CaO for 2002-03
209 crystals. BCR-2G, GSD-1G and BHVO-2G glass reference materials were routinely
210 measured during analytical sessions to monitor data quality (Table S2). For the first mapping
211 technique described (regular mapping), accuracy was better than 10 % and precision was
212 better than 5 %. For the fast-mapping technique, accuracy was better than 15 % and precision
213 was better than 7 %. Trace element concentrations were extracted using the Monocle add-on
214 for Iolite, using the ‘from selections’ option (Petrus et al., 2017). We extracted data from
215 individual hourglass and prism sectors from Cr-rich mantles recording mafic rejuvenation
216 (e.g., Ubide and Kamber, 2018). We used Cr and Zr compositional maps to locate and extract
217 data from hourglass and prism sectors within mantle zones. We also used Ca maps to ensure
218 that cracks and inclusions were avoided. Trace element data for the 1974 microphenocryst are
219 from Ubide et al. (2019a).

220 **3. Results**

221 **3.1. Clinopyroxene Cr-rich mantles**

222 The clinopyroxene crystals analysed in this study are euhedral titanaugites, ranging in sizes
223 from megacrysts (8 – 12 mm length), to phenocrysts (1 – 4 mm) and microphenocrysts (350 –

224 800 μm ; Fig. S1), and classify as diopside-augites following the classification scheme of
225 Morimoto (1988; Fig. S2b). All crystals are sector-zoned, with Cr-rich mantles and Cr-poor
226 outermost rims which transect the sectors (see Fig. 2, Fig. S3). Many crystals also contain
227 cores (Fig. 2), which are resorbed to variable degrees, and may also be sector-zoned. We
228 focus on Cr-rich mantles to explore the development of sector zoning associated with mafic
229 rejuvenation across crystal sizes and eruption types, noting that in the 2002-03 eruption,
230 clinopyroxene with Cr-rich mantles is more common in eccentric samples than in central
231 conduit samples (Magee et al., 2021; Fig. S4). Although the Cr-poor outermost rims may also
232 be sector-zoned, many crystals from the 1974 and 2002-03 eccentric activity only have very
233 thin rims ($< 35 \mu\text{m}$ in prism sectors), hindering analysis and a comprehensive comparison
234 across eruption types and crystal sizes.

235 We compare major and minor element compositions collected from 1669 hourglass and prism
236 sectors in Cr-rich mantle zones to previously published major element data for sector-zoned
237 crystal mantles from the 1974 and 2002-03 eccentric eruptions (Fig. 3; Ubide et al., 2019a),
238 and a compilation of clinopyroxene compositions from Mt. Etna from GEOROC
239 (<https://georoc.eu>; Table S5). Data collected for the 1669 megacrysts is provided in Table S3,
240 and previously published data in Table S4. Broadly, hourglass sectors have higher Mg#,
241 expressed as $\text{MgO} / (\text{MgO} + \text{FeO}_t) \times 100$ on molar basis, and lower $^{\text{T}}\text{Al}$ and $^{\text{M1}}\text{Ti}$ contents
242 than corresponding prism sectors. This compositional variation leads to an increase of T_s in
243 prism sectors at the expense of Di , following Eq (2). On the other hand, $^{\text{M2}}\text{Ca}$ and $^{\text{M2}}\text{Na}$
244 remain constant across sectors for all crystal sizes and eruptions, consistent with previous
245 studies regarding the incorporation of major elements across clinopyroxene sectors at Mt.
246 Etna (Downes 1974, Duncan and Preston 1980, Ubide et al., 2019a; Mollo et al., 2023), and
247 for augitic clinopyroxenes in other systems (Hollister and Gancarz 1971, Leung 1974).
248 In general, clinopyroxene compositions studied here are similar to those previously published

249 at Mt. Etna (Fig. 3). Clinopyroxene mantles from the 1669 eruption have higher ^{M2}Na and
250 lower ^{T}Al and ^{M1}Ti contents than clinopyroxene mantles with the same Mg# from the 1974
251 and 2002-03 eccentric eruptions. Interestingly, the average ^{T}Al content shows that prism
252 sectors in the 1669 megacrysts is lower (0.19 ± 0.01 apfu) than in prism sectors in 1974
253 microphenocrysts (0.28 ± 0.04 apfu) and 2002-03 phenocrysts (0.22 ± 0.02 apfu). In contrast,
254 hourglass sectors in the 1669 megacrysts have ^{T}Al contents (0.15 ± 0.02 apfu) comparable
255 with those from 1974 (0.14 ± 0.02 apfu) and 2002-03 (0.13 ± 0.02 apfu). This effect is
256 illustrated with kernel density estimates in Fig. 4, and suggests that the decrease in crystal
257 size, inferred to reflect increasing nucleation rate at the expense of growth rate upon larger
258 ΔT , results in an increasing departure of prism compositions from hourglass sectors.

259 **3.2. Trace element compositional mapping**

260 LA-ICP-MS trace element maps of clinopyroxene megacrysts, phenocrysts and
261 microphenocrysts highlight the distinct distribution of trace elements between sectors across
262 the range of eruptions and crystals sizes studied (Fig. 2; compositional data in Table S6 and
263 additional maps in Fig. S4). The concentration of HFSE (e.g., Zr and Ta) and REE (e.g., Ce
264 and Yb) follows Al zoning, with higher concentrations in prism sectors compared to
265 hourglass sectors, according to charge balance substitutions previously highlighted in natural
266 and experimental studies (Ubide et al., 2019a; Di Fiore et al., 2021; MacDonald et al., 2022).
267 Importantly, we observe that sector partitioning dominates across a range of eruption styles
268 and crystal sizes at Mt. Etna.

269 Trace element maps also reveal that Cr zoning is mainly concentric and associated with mafic
270 rejuvenation, with comparatively minor partitioning between sectors (Fig. 2). Concentric
271 zones in these crystals crosscut hourglass and prism sectors, highlighting coeval growth of
272 Cr-rich mantle zones across clinopyroxene sectors. The arrival of hot, mafic magma into the
273 system causes resorption of cores and growth of Cr-rich mantle zones (Streck, 2008; Ubide

274 and Kamber, 2018). Across the range of crystals analysed in this study, the degree of Cr
275 enrichment in mantle zones varies from 240 to 1265 ppm in prism sectors, attesting to
276 variable degrees of mafic rejuvenation across eruptions (e.g., Ubide and Kamber 2018) and
277 spatial variability of mafic invasion and mixing in the reservoir (Cashman and Blundy, 2013;
278 Bergantz et al., 2015; Magee et al., 2020). In addition, many crystals from the 2002-03
279 central conduit eruption may not record mafic rejuvenation and hence not contain mantle
280 zones following the definition used here (e.g., Fig. S4), supporting the notion of mafic
281 intrusions being diluted through the central conduits and more effectively tapped through
282 eccentric dykes at Mt. Etna (Clocchiatti et al., 2004; Ubide and Kamber, 2018; Magee et al.,
283 2021) and other mafic volcanoes (e.g., Ubide et al., 2023).

284 **4. Discussion**

285 **4.1. Sector zoning across variable magmatic pathways and crystal sizes**

286 Our set of crystals encompass a range in crystal sizes and eruption types at Mt. Etna,
287 providing a natural dataset to test the relationship between magma undercooling and the
288 extent of sector zoning in clinopyroxene. Different eruptive pathways may be associated with
289 variable magmatic conditions, including temperature, pressure, crystal residence time and
290 ascent, degassing, and cooling rate (Armienti et al., 2013; Kahl et al., 2015). Magma
291 dynamics modulate ΔT and hence, the composition, texture, and development of sector
292 zoning of clinopyroxene (Mollo et al., 2013, 2023; Ubide et al., 2019a; Masotta et al., 2020).
293 In addition to magma ascent pathways, the range of crystal sizes across our suite of samples
294 also attest to differences in clinopyroxene growth rates, with increasing ΔT promoting crystal
295 nucleation over growth, leading to the formation of smaller crystals (Kouchi et al., 1983;
296 Mollo and Hammer, 2017; Masotta et al., 2020; Moschini et al., 2021).

297 As observed in trace element maps (Fig. 2), relative enrichments in HFSE + REE in prism
298 relative to hourglass sectors are directly controlled by Equation (1), which is energetically

299 more favourable in trachybasaltic systems than mechanisms relevant to aegirine-rich
300 clinopyroxenes in highly alkaline magmas (Beard et al., 2019; Bernard et al., 2020). The
301 observed sector partitioning is typical of sector zoning at Mt. Etna and other mafic alkaline
302 settings (Nakamura, 1973; Ubide et al., 2019a, 2019b) and has been shown experimentally to
303 be influenced by ΔT (Grove and Bence, 1979; Kouchi et al., 1983; Mollo et al., 2013, 2018,
304 2023; Masotta et al., 2020; MacDonald et al., 2022). Due to the influence of ${}^{\text{T}}\text{Si} \leftrightarrow {}^{\text{T}}\text{Al}$
305 substitution on the uptake of trace cations, we first investigate the distribution of ${}^{\text{T}}\text{Al}$ between
306 sectors and then explore the degree of enrichment of trace cations in prism relative to
307 hourglass sectors, which we hereafter refer to as ‘sector enrichment.’
308 The difference in ${}^{\text{T}}\text{Al}$ between hourglass and prism sectors differs significantly between
309 samples (Fig. 4). Megacrysts from the 1669 eruption have the lowest difference in ${}^{\text{T}}\text{Al}$ across
310 sectors ($\Delta {}^{\text{T}}\text{Al} = 0.04$ apfu), followed by phenocrysts from the 2002-03 eccentric eruption
311 ($\Delta {}^{\text{T}}\text{Al} = 0.09$ apfu) and microphenocrysts from the 1974 eccentric eruption ($\Delta {}^{\text{T}}\text{Al} = 0.14$
312 apfu). Hourglass sectors define similar ${}^{\text{T}}\text{Al}$ peaks (Fig. 4), but prism sectors define distinct
313 ${}^{\text{T}}\text{Al}$ peaks across clinopyroxene sizes (Fig. 4). Prism ${}^{\text{T}}\text{Al}$ contents and the difference between
314 prism and hourglass compositions, increase with decreasing crystal size, and therefore
315 inferred increasing ΔT (e.g., Mollo and Hammer, 2017). It follows that ${}^{\text{T}}\text{Al}$ sector enrichment
316 reflects key differences in crystallisation conditions associated with mafic rejuvenation events
317 across eruptions.
318 To further explore the degree of sector zoning across samples and quantify its relationship
319 with ΔT , we focus on trace element partitioning between sectors (Fig. 5). Previous works
320 based on natural (Ubide et al., 2019a) and experimental (MacDonald et al., 2022)
321 observations of sector-zoned clinopyroxene from Mt. Etna suggested that the degree of sector
322 enrichment of trace elements in prism relative to hourglass sectors may be a proxy for magma
323 ΔT . To quantify the degree of sector enrichment of a cation, we divide the concentration of

324 that cation in the prism sector by that of the hourglass sector $\{h k 0\}/\{-1 1 1\}$, previously
325 defined as enrichment factor in Shimizu (1981) and then applied to clinopyroxene
326 microphenocrysts from Mt. Etna (Ubide et al., 2019a) and other tectonic settings (Wang et
327 al., 2022). We compare the degree of sector enrichment to the ionic potential of a cation
328 (Z/r^2), where Z is the charge of the cation and r is the ionic radius from Shannon (1976) (Fig.
329 5; Table S7). For a given crystallographic site, the increase in ionic potential correlates with
330 enhanced development of sector zoning, as quantified by the increase in sector enrichment
331 (Fig. 5a).

332 Cations with low ionic potential in M1 and M2 sites (i.e., low charge cations Li, Na, Ni and
333 Sr) are typically not sector-zoned due to their inefficiency as charge balancing cations (Fig. 5;
334 Ubide et al., 2019a). In addition, the degree of sector enrichment of these low-charge cations
335 does not systematically vary between different crystal sizes and eruptions, despite differences
336 in ${}^T\text{Al}$ content and sector zoning (Fig. 4).

337 Following the IUPAC definition for Sc as a transition metal (i.e., an element forming ions
338 with partially filled d orbitals in common settings), we note that Sc and Cr (M1 site) are
339 weakly partitioned between hourglass and prism sectors. Crystal field effects may be more
340 influential in the incorporation of Cr in clinopyroxene compared to local charge balance
341 mechanisms associated with ${}^T\text{Si} \leftrightarrow {}^T\text{Al}$ substitutions (Di Fiore et al., 2021; Mollo et al.,
342 2023), resulting in the relative insensitivity of Cr to sector zoning.

343 As the ionic potential increases from tetravalent HFSE (Zr, Hf) to pentavalent HFSE (Ta, Nb)
344 cations in the M1 site, the degree of sector enrichment increases from megacrysts to
345 microphenocrysts (Fig. 5a). The relationship between crystal size and sector enrichment
346 broadly holds for HFSE as a function of ${}^T\text{Al}$ incorporation in prism and hourglass sectors
347 (Fig. 4). Ta is more variable than tetravalent HFSE across our samples due to its higher
348 charge (see MacDonald et al., 2022), with average enrichment factors ranging between $4.5 \pm$

349 0.8 (1974 microphenocrysts) and 1.9 ± 0.01 (1669 megacrysts). In comparison, Zr has
350 enrichments factors which vary from 2.1 ± 0.2 (1974 microphenocrysts) to 1.4 ± 0.02 (1669
351 megacrysts). The contrast between tetravalent and pentavalent HFSE highlights the effect of
352 ionic charge on sectoral partitioning, as previously suggested by Ubide et al., (2019a).

353 The isoivalent REE series (M2 site) is expanded in Fig. 5b to explore differences in sector
354 enrichment across crystal populations and eruption types. The 1974 microphenocrysts exhibit
355 the highest degree of sector enrichment of our sample set, in accordance with the highest ${}^T\text{Al}$
356 contrast between sectors (Fig. 4). This attests to the importance of charge-balancing
357 substitution mechanisms in the uptake of REE into the M2 site, as the probability of REE
358 entering a charge-neutral site increases with increasing ${}^T\text{Al}$ (Blundy et al., 1998; Hill et al.,
359 2000; Wood and Blundy, 2001; Mollo et al., 2013, 2018, 2020). With the increase in size
360 from 2002-03 phenocrysts to 1669 megacrysts, sector enrichment decreases across the REE
361 (Fig. 5b), supporting the link between undercooling, growth rate and trace element
362 incorporation.

363 We note that sector enrichment decreases with ionic potential from light to heavy REE, with
364 higher variability of LREE (e.g., La, Ce) across crystal sizes and samples compared to HREE
365 (e.g., Lu, Y in Fig. 6). This suggests that HREE may be less influenced by the entry of ${}^T\text{Al}$,
366 compared to LREE, as previously observed in experimental studies (MacDonald et al., 2022).

367 Average sector enrichments for La and Lu (as proxies for LREE and HREE respectively) are
368 stronger in the 1974 microphenocrysts (La = 1.8 ± 0.1 , Lu = 1.5 ± 0.2) than in 2002-03
369 phenocrysts (La = 1.6 ± 0.05 , Lu = 1.4 ± 0.1) and 1669 megacrysts (La = 1.3 ± 0.04 , Lu =
370 1.2 ± 0.04), which potentially crystallised under decreasing ΔT .

371 In summary, as the difference in ${}^T\text{Al}$ between sectors increases, HFSE and REE are more
372 enriched in prism sectors relative to simultaneously growing hourglass sectors, resulting in
373 higher degrees of sector enrichment. To explore the relationship between sector enrichment

374 and crystallisation dynamics associated with pre-eruptive mafic rejuvenation, influencing
375 crystal size and the development of sector zoning in our crystals, we plot the sector
376 enrichments of a range of HFSE and REE against crystal width in Fig. 6.

377 Crystallographic contrasts in sector-zoned clinopyroxene in mafic alkaline systems reflect the
378 interplay of relative growth rates between sectors, diffusion of cations in the melt and
379 geometric distribution of lattice sites between crystal faces as induced by ΔT , causing the
380 development of compositionally distinct local melts which feed crystal growth (Hollister and
381 Gancarz, 1971; Nakamura, 1973; Downes, 1974; Leung, 1974; Dowty, 1976; Mollo et al.,
382 2023). Specifically, the preferential uptake of Si and Mg in hourglass $\{-1\ 1\ 1\}$ sectors in
383 augitic clinopyroxene can be attributed to the simultaneous exposure of M and T sites,
384 requiring both divalent cations and silica tetrahedra (Nakamura 1973; Leung, 1974),
385 ultimately resulting in the depletion of Si and Mg and enriched in cations such as Al and Ti in
386 the melt adjacent to hourglass sectors (Leung, 1974). On the other hand, prism $\{h\ k\ 0\}$ sectors
387 have alternating exposed layers of M and T sites, therefore requiring large amounts of these
388 cations to facilitate growth, enabling the accommodation of cations such as Al and Ti and
389 ultimately causing their depletion in the melt adjacent to prism sectors (Nakamura, 1973;
390 Leung, 1974). Importantly, when T site layers are exposed, rapid depletion of Si in the local
391 melt results in its substitution with Al, and this effect is enhanced in undersaturated liquids
392 (Leung, 1974). Following this principle, the degree of sector enrichment of Al and
393 subsequently, HFSE and REE, is expected to increase with ΔT (Mollo et al., 2023).

394 Under kinetic growth conditions, crystal growth is driven by ΔT , which approximates melt
395 supersaturation phenomena arising from concentration-dependent reactions induced by
396 interface kinetics (Mollo and Hammer, 2017). Therefore, initial concentration gradients in the
397 melt at the crystal-melt interface are counterbalanced by diffusive relaxation that becomes
398 more effective over crystallisation timescales (i.e., the crystal residence time). Following this

399 logic, the growth rate of clinopyroxene decreases as the crystal residence time increases and
400 approaches zero as the melt relaxes towards an equilibrium state where concentration
401 gradients cease (Pontesilli et al., 2019; Moschini et al., 2021). Decreasing ΔT promotes a
402 decrease in maximum crystal growth rate, leading to a steady-state textural maturation of
403 polyhedral crystal forms (Mollo and Hammer, 2017). The combination of long residence
404 times and low ΔT mitigates the compositional contrast between melts feeding the growth of
405 different crystal faces, thereby lowering the degree of sectoral enrichment in clinopyroxene.
406 The growth of clinopyroxene megacrysts erupted during the 1669 eruption are frequently
407 attributed to long residence times, typical of 17th century activity at Mt. Etna (Viccaro et al.,
408 2016; Magee et al., 2020). Indeed, estimated crystal residence times associated with the
409 growth of Cr-rich mantles are longer (22 ± 2 days; Magee et al., 2020) than those from recent
410 activity (6 ± 4 days for eruptions from 1974 to 2014; Ubide and Kamber, 2018). Our results
411 indicate that decreasing crystal width and shorter residence times are associated with stronger
412 sector enrichments for HFSE and REE, from 1669 megacrysts to 2002-03 phenocrysts and
413 1974 microphenocrysts. Below, we explore the relationship between ΔT , growth rates and
414 residence time. We quantify ΔT and discuss implications for mafic rejuvenation, mush
415 remobilisation and the onset of magma ascent along distinct pathways.

416 **4.2. Quantifying magma undercooling**

417 Magma undercooling exerts a significant control on the final composition and texture of
418 clinopyroxene crystals (Kouchi et al., 1983; Mollo and Hammer, 2017; Masotta et al., 2020;
419 MacDonald et al., 2022). As we note previously, the degree of sector enrichment in our
420 crystals appears to be related to crystal growth rate and in turn to residence time and ΔT
421 (Pontesilli et al., 2019; Moschini et al., 2021). Here, we use the ΔT model based on REE
422 clinopyroxene-melt partitioning calibrated by MacDonald et al. (2022) to quantify magma ΔT
423 associated with Cr-rich mantle zones. We calculate ΔT based on hourglass compositions, as

424 the preferential uptake of REE in prism sectors leads to erroneously high ΔT (MacDonald et
425 al., 2022).

426 The model calibration dataset uses experimental crystals synthesised from a mafic Etna
427 trachybasalt composition (MacDonald et al., 2022), applicable to crystals from the 1974 and
428 2002-03 eruptions. Although the 1669 lavas are trachybasalts and have compositions similar
429 to those produced experimentally for the REE model (Fig. S2b), clinopyroxene compositions
430 deviate slightly from the general Etna trend (Fig. 3), and protracted crystal growth and
431 storage attributed to megacrysts (Magee et al., 2021) complicates the identification of an
432 appropriate liquid composition to calculate apparent partition coefficients. Additionally, the
433 crystals used to produce the REE calibration are considerably smaller (250 μm width for
434 sector-zoned crystals) than the megacrysts, highlighting that this model is likely not suitable
435 the presumably lower ΔT related to megacrysts at Mt. Etna. Calculated ΔT for the 1974
436 crystals were previously reported in MacDonald et al. (2022), where REE apparent partition
437 coefficients were determined by using a hand-picked groundmass composition for the melt
438 (Magee et al., 2021). For the 2002-03 eccentric and central conduit melt compositions, we
439 use the handpicked groundmass compositions (eccentric: 15-TU-106, central conduit: 16-SF-
440 212) by Magee et al. (2021). Melt compositions and apparent partition coefficients are
441 reported in Table S8.

442 Prior to calculating ΔT , we test whether the apparent partition coefficients are indicative of
443 near-equilibrium crystallisation conditions by the attainment of a local thermodynamic
444 equilibrium at the crystal-melt interface. Following the guidelines set out by MacDonald et
445 al. (2022), we plot Onuma curves for apparent partition coefficients from hourglass sectors to
446 ensure that the uptake of REE into the M2 site of clinopyroxene follows thermodynamic
447 principles for the partitioning energetics of trace cation substitutions (Onuma et al., 1968;
448 Brice, 1975; Blundy and Wood, 1994). The logarithm of apparent partition coefficients from

449 the 1974 and 2002-03 eruptions shows near-parabolic relationships with cation ionic radius,
450 as the lattice strain energy exerts an overarching control on REE incorporation into the lattice
451 site (Fig. S5). This excludes strong disequilibrium uptake of REE under conditions of high
452 melt supersaturation (Mollo and Hammer, 2017). Indeed, near-equilibrium crystallisation
453 conditions agree with the polyhedral morphology of clinopyroxene in our samples (Fig. S1).
454 On average, our ΔT estimates are below the threshold for sector-zoned clinopyroxene
455 determined by experimental studies ($\Delta T < 45$ °C; Kouchi et al., 1983, Masotta et al., 2020;
456 Fig. 7; Table S7). The average ΔT of all crystals fall within the model uncertainty (± 12 °C),
457 suggesting that conditions of mafic rejuvenation may be similar regardless of eruption type. It
458 is important to note that this ΔT model is calibrated on compositions of clinopyroxene which
459 crystallised at ΔT ranging from 23 to 173 °C, with polyhedral, sector-zoned crystals formed at
460 the lower end of the ΔT range ($\Delta T = 23 - 32$ °C) and higher undercoolings leading to skeletal
461 ($\Delta T = 75 - 123$ °C) and dendritic ($\Delta T = 132 - 173$ °C) crystals (MacDonald et al., 2022).
462 Hence, this calibration may not be sufficiently sensitive to distinguish between low and only
463 discreetly different ΔT . Despite this model limitation, inspection of ΔT kernel density
464 estimates does suggest that Cr-rich microphenocryst mantles from the 1974 eruption are
465 associated with slightly higher ΔT ($\Delta T = 41 \pm 6$ °C) than 2002-03 eccentric ($\Delta T = 31 \pm 11$ °C)
466 and central conduit ($\Delta T = 30 \pm 6$ °C) phenocryst mantles, which are almost indistinguishable
467 from one another (Fig. 7). The 1974 microphenocrysts show highest sector enrichments for
468 both ^{27}Al (Fig. 4) and trace elements (Fig. 5), suggesting they may have indeed crystallised
469 under the effect of more dynamic mafic rejuvenation, mush remobilisation and onset of
470 ascent relative to 2002-03 phenocrysts.

471 For comparison, we also calculate ΔT using the clinopyroxene-only major element calibration
472 of Masotta et al., (2020), based on the same series of experiments but without the requirement
473 of a representative equilibrium melt composition, which is a limitation of the REE

474 partitioning model by MacDonald et al., (2022; Fig. 7). Results from the clinopyroxene major
475 element model are within model uncertainty ($\pm 22^\circ\text{C}$) of each other for our data set.

476 However, phenocrysts from the 2002-03 eccentric eruption typically return lower ΔT (41 ± 16
477 $^\circ\text{C}$) than microphenocrysts from the 1974 eccentric eruption ($\Delta T = 47 \pm 19$ $^\circ\text{C}$), similar to the
478 results obtained using the REE clinopyroxene-melt partitioning model (Fig. 7). We note that
479 both ΔT models are calibrated on single bulk compositions (Fig. S2a), limiting their
480 application to other volcanic systems, yet return adequate results across our data set.

481 There are remarkably minimal differences in sector zoning between phenocryst mantles from
482 the eccentric and central conduit 2002-03 eruptions. The similarity in ΔT estimates (Fig. 7)
483 and sectoral enrichments of trace cations (Fig. 5) suggest that crystallisation of mantle zones
484 and formation of sector zoning occurred under comparable conditions. Thus, clinopyroxene
485 phenocrysts were recycled from compositionally similar mushes, regardless of final ascent
486 pathway, with the main difference being the commonality of sector-zoned crystals in
487 eccentric samples relative to their rarity in central conduit samples, which attests to the higher
488 complexity of magma ascent through central conduits at Mt. Etna (Ubide and Kamber, 2018;
489 Magee et al., 2021). If this interpretation is correct, then the outermost Cr-poor rim,
490 crystallised upon ascent (Ubide and Kamber, 2018) may hold differences between eruption
491 pathways, with central conduit ascent linked to lower ΔT than eccentric ascent.

492 Unfortunately, most clinopyroxene phenocrysts from the 2002-03 eccentric eruption have
493 minimally developed Cr-poor outermost rims (< 35 μm in prism sectors), too thin for reliable
494 data from both hourglass and prism sectors to be extracted. In contrast, rims from the 2002-
495 03 central conduit eruptions can be much larger (> 84 μm in prism sectors) and in some
496 cases, entire phenocrysts are Cr-poor (Fig. S4), as expected from limited sampling of mafic
497 intrusions at depth due to more complex connections between magma reservoirs and longer
498 crystal residence times relative to eccentric eruptions (Kahl et al., 2015).

499 Finally, we explore the relationship between ΔT estimates based on REE partitioning and
500 concentrations in other trace elements in hourglass zones (Fig. 8). Experimental studies
501 highlight the link between ΔT and REE + HFSE in clinopyroxene, whilst low charge cations
502 such as large ion lithophile elements (LILE) are relatively unaffected (Mollo et al., 2013;
503 MacDonald et al., 2022). Hence, it would be expected that for natural crystals, ΔT should
504 only be weakly related to cations with low ionic potential and correlated with those with high
505 ionic potential. Following this, the concentration of monovalent cations such as Li is
506 unrelated to ΔT estimates (Fig. 8). Transition metals with low ionic potential and high crystal
507 field stabilisation energy such as Cr are also relatively unaffected by ΔT , further reinforcing
508 its low sensitivity to crystallisation kinetics. In contrast, HFSE are positively correlated with
509 ΔT , validating our proposal that the enrichment of cations with high ionic potential in prism
510 relative to hourglass sectors can be used to track ΔT and therefore the dynamic crystallisation
511 histories of magma. This is consistent with similar incorporation mechanisms governing the
512 uptake of both HFSE and REE in clinopyroxene from different eruptions at Mt. Etna. Minor
513 deviations from the correlation between ΔT and Ta (Fig. 8) are likely due to the analytical
514 limitations associated with measuring the naturally low concentration of Ta in clinopyroxene.
515 Further work combining ΔT estimates and sector enrichment, in conjunction with other tools
516 such as crystal size distributions (Moschini et al., 2021) may be pivotal in further unravelling
517 magma dynamics associated with magma recharge and ascent.

518 **4.3 Implications for magma dynamics**

519 Our work shows that the degree of sector enrichment in clinopyroxene reflects variations in
520 magma undercooling and may provide insights into pre-eruptive dynamics associated with
521 magma storage, mixing, mush disaggregation and the onset of ascent in alkaline systems.
522 Here, we link our results with pre-eruptive dynamics for each eruption to highlight the
523 potential of exploring sector zoning as a recorder of magmatic processes and discuss

524 implications for other volcanic settings and magma chemistries in the following section.

525 We first consider the 1669 flank eruption, the most voluminous and destructive in recorded
526 history at Mt. Etna, which heralded the conclusion of the 17th century eruption period,
527 characterised by high effusion rates and long-lived volcanic activity (Condomines et al.,
528 1995; Corsaro et al., 1996; Branca et al., 2013). Clinopyroxene megacrysts from the 1669
529 eruption exhibit weaker sector zoning in Cr-rich mantles than phenocrysts and
530 microphenocrysts from recent eruptions (Fig. 5), possibly reflecting longer residence times in
531 a crystallisation regime where growth was preferred over nucleation (low ΔT). Growth under
532 initially high ΔT followed by prolonged storage can be discounted as these crystals do not
533 exhibit textures indicative of initial growth under diffusion-controlled regimes (i.e., skeleton-
534 overgrowth textures; Pontesilli et al., 2019). The high effusion rate of 17th century activity at
535 Mt. Etna has been attributed to the development of long-lived magma reservoirs leading to
536 protracted crystal growth in comparison to recent activity (Armienti et al., 1997; Viccaro et
537 al., 2016). Cr-rich mantles in 1669 clinopyroxene are interpreted as recorders of eruption
538 triggering ‘cryptic’ recharge (Magee et al., 2020). Sustained magma flux can lead to the
539 crystallisation of megacrysts in volcanic systems (Landi et al., 2019), and mildly sector-
540 zoned clinopyroxene megacrysts from Stromboli are interpreted to record protracted storage
541 and convection at the edges of melt-dominated magmatic reservoirs, inducing low ΔT (Ubide
542 et al., 2019b). Indeed, stirring experiments show convective mixing can enhance
543 clinopyroxene crystallisation and limit kinetic effects, such as the development of sector
544 zoning (Di Fiore et al., 2021). Hence, crystallisation of 1669 Cr-rich mantles may have taken
545 place under conditions of low ΔT , where convection enhanced crystal growth and diminished
546 the extent of sector zoning.

547 Recent (post 1970) activity at Mt. Etna is more closely associated with a ‘steady-state’
548 plumbing system with more frequent eruptions, smaller erupted volumes and shorter crystal

549 residence times (Behncke and Neri, 2003; Clocchiatti et al., 2004; Viccaro et al., 2016).
550 Reflecting this, the magnitude of sector enrichment in clinopyroxene microphenocrysts and
551 phenocrysts from the 1974 and 2002-03 eruptions, respectively, indicates that these Cr-rich
552 mantles crystallised under higher ΔT conditions than those of Cr-rich mantles in megacrysts
553 from the 1669 eruption (Fig. 5). We infer that the stronger sector zoning of Cr-rich mantles in
554 the phenocrysts and microphenocrysts indicates processes of mush disaggregation by mafic
555 rejuvenation events triggering the onset of magma ascent. Comparison of the two eruptions
556 also reveals interesting, albeit subtle distinctions (Fig. 7). The 1974 microphenocrysts record
557 slightly higher sector enrichment and ΔT , suggestive of more rapid recharge, mush
558 remobilisation and initiation of ascent compared to the 2002-03 phenocrysts. Ten days prior
559 to the 1974 eruption, Mt. Etna experienced its most intense seismic crisis recorded (Bottari et
560 al., 1975), which has been interpreted to signify the intrusion of eruption triggering mafic
561 magma (Corsaro et al., 2009; Ubide and Kamber, 2018). In contrast, the 2002-03 eruption
562 was preceded by longer (8 weeks) and relatively less intense seismicity (Gambino et al.,
563 2004). In line with this, clinopyroxene growth timescales are longer in 2002-03 relative to
564 1974 crystals (Ubide and Kamber 2018), and diffusion chronometry in olivine, constrains
565 mafic rejuvenation prior to the 2002-03 eruption at 44 ± 22 days (Kahl et al., 2015). The
566 longer time between recharge and eruption for the 2002-03 products is consistent with
567 slightly lower ΔT and hence larger crystal sizes and weaker sector enrichment of Cr-rich
568 mantles compared to 1974 products, which document vigorous mixing and fast
569 remobilisation to ascent with limited storage.

570 **4.4. The role of melt geochemistry and magma undercooling on sector zoning across** 571 **magmatic settings and compositions**

572 Sector zoning in clinopyroxene has been identified across a range of volcanic settings,
573 including mid ocean ridges (Neave et al., 2019), arcs (Arculus, 1973; Brophy et al., 1999;
574 Ubide et al., 2019b), continental hotspots (Tapu et al., 2022), oceanic hotspots (Ubide et al.,
575 2023), and in post-collisional systems (Zhou et al., 2021). Sector zoning may be broadly split
576 by geochemical affinity; in tholeiitic systems, Na and Ca may also be preferentially
577 incorporated into prism sectors alongside Al + Ti (Nakamura, 1973; Neave and Putirka,
578 2017; Neave et al., 2019), whereas in alkaline settings, Ca and Na are not strongly distributed
579 between sectors (Ubide et al., 2019a, 2019b). To test the degree of sector enrichment as a
580 recorder of dynamic pre-eruptive histories, and the potential effect of variations in melt
581 composition on sector zoning across alkaline systems, we examine sector enrichment of ^TAl
582 in clinopyroxene phenocryst from the La Palma 2021 eruption (Canary Island ocean island
583 basalts) published in Ubide et al (2023) and megacrysts from Roman era activity (2.4 – 1.8
584 ka; “Pizzo activity”) at Stromboli volcano (data from Ubide et al., 2019b; Table S9; Fig. 9).
585 Throughout the duration of the La Palma 2021 eruption, tephrite to basanite lavas were
586 produced from the main fissure (“central cone”). Towards the end of the eruption, basanite
587 lavas were also produced episodically from fissures located several kilometres away from the
588 central cone, which are termed “eccentric” by Ubide et al. (2023). Clinopyroxene from the
589 2021 La Palma eruption contain ubiquitous ‘inner rims’ (equivalent to our ‘mantles’), which
590 are sector-zoned and enriched in Cr₂O₃ and Mg# relative to neighbouring crystal zones,
591 recording the onset of eruption triggering mafic rejuvenation and mush disaggregation at
592 upper mantle depths (Ubide et al., 2023). Similarly, Stromboli clinopyroxene megacrysts
593 erupted from the Pizzo shoshonite scoria cone in Roman times, are comprised of Cr-rich
594 mantle zones which transect hourglass and prism sectors (Ubide et al., 2019b). Both studies
595 provide compositional data that are texturally constrained in respect to both oscillatory and
596 sector zoning, affording a direct comparison with our Mt. Etna data.

597 Hourglass and prism sectors contain the highest ^TAl in clinopyroxene crystals from La Palma,
 598 followed by Mt. Etna, and finally, Stromboli (Fig. 9b-d). We assess the effect of melt
 599 composition on clinopyroxene ^TAl , using groundmass data as a representative of eruption
 600 melt (Magee et al., 2021; Ubide et al., 2023; Fig. 9a). La Palma melts are more alkaline and
 601 SiO_2 undersaturated than Etna and Stromboli melts, with higher melt Ti contents (Table 1),
 602 which may enhance the uptake of ^TAl into clinopyroxene lattice sites (Sack and Carmichael,
 603 1984). Furthermore, undersaturated melts with low silica activity may also promote the
 604 uptake of ^TAl (Leung, 1974). Interestingly, increasing melt alkalinity has been associated
 605 with decreased ^TAl in aegirine from strongly alkaline melts (Beard et al., 2019), which is not
 606 observed for the titanagites from less extreme alkaline compositions explored (Fig. 9a). Melt
 607 compositions from Stromboli have the highest Si/Al and lowest TiO_2 (Table 1). The greater
 608 availability of Si in the melt may potentially hinder the uptake of ^TAl in clinopyroxene,
 609 ultimately resulting in the significant contrasts observed here. Alternatively, Al may be more
 610 preferentially incorporated into clinopyroxene at increasing pressures (Müntener et al., 2001),
 611 however, crystallisation pressures of Cr-rich clinopyroxene mantles are similar for La Palma
 612 (529 ± 150 MPa; Ubide et al., 2023), Mt. Etna (e.g., 1669 megacrysts between 400 – 500
 613 MPa; Magee et al., 2020) and Stromboli (316 ± 33 MPa; Ubide et al., 2019b). This suggests
 614 that melt composition is more likely to influence clinopyroxene ^TAl .

	Melt Al_2O_3 (wt. %)	Melt SiO_2 (wt. %)	Melt TiO_2 (wt. %)	Melt Si/Al	^TAl (cpx hourglass)	^TAl (cpx prism)
1669 Etna	19.06	48.65	1.74	2.55	0.15	0.19
1974 Etna	16.42	45.87	1.87	2.79	0.14	0.28
2002 Etna (eccentric)	18.10	48.86	1.70	2.70	0.13	0.22
La Palma	15.90	45.64	3.72	2.87	0.21	0.32
Stromboli	15.00	51.06	1.48	3.41	0.11	0.14

615 Table 1: Melt compositions for selected elements from Mt. Etna (Magee et al., 2020, 2021),
 616 Stromboli (Ubide et al., 2019b) and La Palma (Ubide et al., 2023) groundmass, with average
 617 ^TAl for clinopyroxene hourglass and prism sectors. Cpx = clinopyroxene.

618 In contrast, sector enrichment (e.g., $\Delta^T\text{Al}$) is not strongly influenced by melt composition.
619 Megacrysts from Stromboli have the same $\Delta^T\text{Al}$ as megacrysts from the 1669 eruption at Mt.
620 Etna, despite differences in melt composition (Fig. 9), attesting to the limited development of
621 sector zoning and protracted residence times (e.g., Ubide et al., 2019b; Magee et al., 2020).
622 Similarly, phenocrysts from La Palma have $\Delta^T\text{Al}$ comparable to phenocrysts and
623 microphenocrysts from Mt. Etna (Fig. 9b), suggestive of growth associated with mush
624 remobilisation and the onset of magma ascent at $\Delta T < 45$ °C. Comparison of central and
625 eccentric products from La Palma reveal minimal differences in $\Delta^T\text{Al}$, suggestive of similar
626 pre-eruptive magma dynamics associated with magma rejuvenation across eruption pathways,
627 resembling Mt. Etna. Therefore, from these observations, the degree of sector enrichment is
628 comparable for similar crystal populations across different alkaline systems (Fig. 9b),
629 emphasising its potential as an indicator of magma ΔT across magmatic settings.,
630 Overall, our assessment shows that across different mafic alkaline settings (i.e., arc and ocean
631 island basalt), the development of sector zoning in phenocrysts and microphenocrysts is
632 similar. This highlights that although $\Delta^T\text{Al}$ may be influenced by variations in melt
633 compositions across magmatic systems, the development of sector zoning is seemingly
634 unrelated. We stress that for subalkaline compositions, different incorporation mechanisms
635 may be associated with sector zoning (Neave and Putirka 2017; Neave et al., 2019), and
636 further investigations of sector-zoned clinopyroxene from these systems are required to
637 explore this effect. Nonetheless, the framework used here could be applied as a tool to
638 investigate pre-eruptive magma dynamics at other volcanic systems. Further improvements of
639 the geochemical inventory of texturally constrained sector-zoned clinopyroxene,
640 experimental constraints (including further quantifying the role of melt composition), and
641 application of this approach to other natural systems may reveal further insights into pre-
642 eruptive dynamics across other volcanic environments.

643 **5. Conclusions**

644 Using major, minor and trace element compositional variations between hourglass and prism
645 sectors in clinopyroxene from a range of eruption types at Mt. Etna, we outline that sector
646 zoning associated with Cr-rich mantle zones provides a detailed record of crystallisation
647 kinetics. Across our entire range of crystal sizes, rare earth elements and high field strength
648 elements are enriched alongside tetrahedral aluminium in prism sectors relative to
649 simultaneously growing hourglass sectors. On the other hand, cations with low charge to
650 ionic radius ratios, such as the large ion lithophile elements, and transition metal cations (e.g.,
651 Cr), are relatively unaffected by the development of sector zoning.

652 The degree of sector enrichment of cations increases with the degree of undercooling. In our
653 samples, sector enrichment is highest for microphenocrysts from the 1974 eccentric eruption,
654 followed by phenocrysts from the 2002-03 eccentric and central conduit eruptions, and
655 lowest for megacrysts from the 1669 flank (central conduit) eruption. We infer that variable
656 crystal sizes across these eruptions reflect differences in crystal growth rates, magma
657 undercooling and residence times, causing a systematic decrease in the development of sector
658 zoning with increasing crystal size. Quantification of undercooling based on clinopyroxene
659 major elements and REE partitioning, highlights that magma undercooling associated with
660 mafic rejuvenation is similar across eruptions ($\Delta T < 45$ °C). However, the combination of
661 undercooling estimates and sectoral enrichment indicates that 1974 eccentric
662 microphenocrysts record higher undercooling than the 2002-03 phenocryst archives,
663 confirming that higher degrees of sectoral enrichment are likely a reflection of more vigorous
664 mafic rejuvenation and initiation of magma ascent. Undercooling and sector zoning are
665 remarkably similar between crystals erupted from the eccentric and central conduit eruptions
666 in 2002-03 at Mt. Etna, attesting to the connectivity of mushes across eruption styles.

667 Integrating our results to explore pre-eruptive dynamics in the 1669, 1974 and 2002-03

668 eruptions, we propose that variable sector enrichment of tetrahedral aluminium, high field
669 strength elements and rare earth elements reflect differences in the dynamics of magmatic
670 environments, including time from recharge to eruption. Comparison with sector-zoned Cr-
671 rich zones from the 2021 La Palma eruption (phenocrysts) and from 2.4 – 1.8 ka Pizzo
672 activity at Stromboli volcano (megacrysts) highlights that sector enrichment varies as a
673 function of crystal size and magma undercooling across different mafic alkaline settings.
674 Importantly, sector partitioning does not appear to be influenced by variations in melt
675 chemistry, which modulates clinopyroxene compositions. Overall, our approach indicates the
676 potential of using the development and magnitude of sector zoning in clinopyroxene to
677 explore magma undercooling and pre-eruptive dynamics in active volcanic settings.

678 **Acknowledgments**

679 This work was supported by a Foundation Research Excellence Award from The University
680 of Queensland, the Advance Queensland Women’s Research Assistance Program from the
681 Queensland Government and an Australian Research Council Discovery Project to T.U. (UQ-
682 FREA RM2019001828, WRAP109-2019RD1 RM2020002371, ARC DP200101566). A.M.
683 was supported by the Australian Government Research Training Program (RTP; PhD
684 scholarship) for the duration of this study. S.M. was supported by “MIUR-PRIN 2022
685 PROVES Project (Grant #2022N4FBAA). We thank Henrietta Cathey for assistance with
686 microprobe analysis at QUT and Jack Ward for support with LA-ICP-MS analysis at UQ. We
687 also thank Jon Blundy and Penny Weiser for their comments and insights on an earlier
688 version of the manuscript., and Jinsheng Zhou, Charles D. Beard, and an anonymous
689 reviewer for their thoughtful comments that materially improved the presentation and
690 discussion of our results. We are very grateful to Rosemary Hickey-Vargas and Jeffrey
691 Catalano for their editorial guidance.

692 **Data Availability**

693 Data are available through Mendeley Data at doi: 10.17632/bhtk35hgxz.3

694 **Appendix A. Supplementary Material**

695 The supplementary figures associated with this paper include photomicrographs and back
696 scattered electron images of clinopyroxene crystals, groundmass and clinopyroxene
697 classification diagrams, additional clinopyroxene LA-ICP-MS compositional maps for Cr and
698 Onuma curves produced for all clinopyroxene crystals, provided in a single PDF file.

699 **References**

- 700 Andronico D., Branca S., Calvari S., Burton M., Caltabiano T., Corsaro R. A., Del Carlo P.,
701 Garfi G., Lodato L. and Miraglia L. (2005) A multi-disciplinary study of the 2002–03
702 Etna eruption: Insights into a complex plumbing system. *Bull. Volcanol.* **67**, 314-330.
- 703 Arculus R. J. (1973) *The alkali basalt andesite association of grenada lesser antilles* PhD
704 Thesis. Durham University.
- 705 Armienti P., Pareschi M. and Pompilio M. (1997) Lava textures and time scales of magma
706 storage at Mt. Etna (Italy). *Acta Vulcan.* **9**, 1-6.
- 707 Armienti P., Tonarini S., Innocenti F. and D Orazio M. (2007) Mount Etna pyroxene as tracer
708 of petrogenetic processes and dynamics of the feeding system. *Geol. Soc. Am. Spec.*
709 *Pap.* **418**, 265-276.
- 710 Armienti P., Perinelli C. and Putirka K. D. (2013) A new model to estimate deep-level
711 magma ascent rates, with applications to Mt. Etna (Sicily, Italy). *J. Petrol.* **54**, 795-
712 813.
- 713 Beard C.D., van Hinsberg V.J., Stix J., Wilke M. (2019) Clinopyroxene/melt trace
714 element partitioning in sodic alkaline magmas. *J. Petrol.* **60**, 1797–1823.
- 715 Bernard C., Estrade G., Salvi S., Béziat D., Smith M. (2020) Alkali pyroxenes and

716 amphiboles: a window on rare earth elements and other high field strength
717 elements behavior through the magmatic-hydrothermal transition of
718 peralkaline granitic systems. *Contrib. Miner. Petrol.* **175**, 1–27.

719 Behncke B. and Neri M. (2003) The July–August 2001 eruption of Mt. Etna (Sicily). *Bull.*
720 *Volcanol.* **65**, 461-476.

721 Bergantz G., Schleicher J. and Burgisser A. (2015) Open-system dynamics and mixing in
722 magma mushes. *Nat. Geosci.* **8**, 793-796.

723 Blundy J. and Wood B. (1994) Prediction of crystal–melt partition coefficients from elastic
724 moduli. *Nature* **372**, 452-454.

725 Blundy J., Robinson J. and Wood B. (1998) Heavy REE are compatible in clinopyroxene on
726 the spinel lherzolite solidus. *Earth Planet. Sci. Lett.* **160**, 493-504.

727 Bottari A., Lo Giudice E., Patanè G., Romano R. and Sturiale C. (1975) L'eruzione etnea del
728 gennaio-marzo 1974. *Riv. Min. Sic* **154**, 175-199.

729 Branca S., De Beni E. and Proietti C. (2013) The large and destructive 1669 AD eruption at
730 Etna volcano: Reconstruction of the lava flow field evolution and effusion rate trend.
731 *Bull. Volcanol.* **75**, 1-16.

732 Brice J. (1975) Some thermodynamic aspects of the growth of strained crystals. *J. Cryst.*
733 *Growth* **28**, 249-253.

734 Brophy J. G., Whittington C. S. and Park Y.-R. (1999) Sector-zoned augite megacrysts in
735 aleutian high alumina basalts: Implications for the conditions of basalt crystallization
736 and the generation of calc-alkaline series magmas. *Contrib. Mineral. Petrol.* **135**, 277-
737 290.

738 Cashman K. and Blundy J. (2013) Petrological cannibalism: The chemical and textural
739 consequences of incremental magma body growth. *Contrib. Mineral. Petrol.* **166**,
740 703-729.

741 Clocchiatti R., Condomines M., Guénot N. and Tanguy J.-C. (2004) Magma changes at
742 Mount Etna: The 2001 and 2002–2003 eruptions. *Earth Planet. Sci. Lett.* **226**, 397-
743 414.

744 Condomines M., Tanguy J.-C. and Michaud V. (1995) Magma dynamics at Mt Etna:
745 Constraints from U-Th-Ra-Pb radioactive disequilibria and Sr isotopes in historical
746 lavas. *Earth Planet. Sci. Lett.* **132**, 25-41.

747 Corsaro R., Métrich N., Allard P., Andronico D., Miraglia L. and Fourmentraux C. (2009)
748 The 1974 flank eruption of Mount Etna: An archetype for deep dike-fed eruptions at
749 basaltic volcanoes and a milestone in Etna's recent history. *J.l of Geophys. Res.: Solid*
750 *Earth* **114**, B07204.

751 Corsaro R. A., Cristofolini R. and Patanè L. (1996) The 1669 eruption at Mount Etna:
752 Chronology, petrology and geochemistry, with inferences on the magma sources and
753 ascent mechanisms. *Bull. Volcanol.* **58**, 348-358.

754 Costa F., Shea T., Ubide T. (2020) Diffusion chronometry and the timescales of magmatic
755 processes. *Nature Rev. Earth & Enviro.* **1**, 201-214.

756 Di Fiore F., Mollo S., Vona A., MacDonald A., Ubide T., Nazzari M., Romano C. and
757 Scarlato P. (2021) Kinetic partitioning of major and trace cations between
758 clinopyroxene and phonotephritic melt under convective stirring conditions: New
759 insights into clinopyroxene sector zoning and concentric zoning. *Chem. Geol.*, 584,
760 120531.

761 Di Stefano F., Mollo S., Ubide T., Petrone C. M., Caulfield J., Scarlato P., Nazzari M.,
762 Andronico D. and Del Bello E. (2020) Mush cannibalism and disruption recorded by
763 clinopyroxene phenocrysts at Stromboli volcano: New insights from recent 2003–
764 2017 activity. *Lithos* **360**, 105440.

- 765 Downes M. (1974) Sector and oscillatory zoning in calcic augites from Mt. Etna, Sicily.
766 *Contrib. Mineral. Petrol.* **47**, 187-196.
- 767 Dowty E. (1976) Crystal structure and crystal growth: II. Sector zoning in minerals. *Am.*
768 *Mineral.* **61**, 460-469.
- 769 Dowty E. (1980) Crystal growth and nucleation theory and the numerical simulation of
770 igneous crystallization. *Physics of Magmatic Processes*. Princeton Univ. Press. pp.
771 419-486.
- 772 Gambino S., Mostaccio A., Patanè D., Scarfi L. and Ursino A. (2004) High-precision
773 locations of the microseismicity preceding the 2002–2003 Mt. Etna eruption.
774 *Geophys. Res. Lett.* **31**.
- 775 Duncan A. M. & Preston R.M.F. (1980) Chemical variation of clinopyroxene phenocrysts
776 from the trachybasaltic lavas of Mount Etna, Sicily. *Min. Magazine.* **43**(330), 765-
777 770.
- 778 Giacomoni P. P., Coltorti M., Bryce J., Fahnestock M. and Guitreau M. (2016) Mt. Etna
779 plumbing system revealed by combined textural, compositional, and
780 thermobarometric studies in clinopyroxenes. *Contrib. Mineral. Petrol.* **171**, 34.
- 781 Grove T. L. and Bence A. Crystallization kinetics in a multiply saturated basalt magma-an
782 experimental study of Luna 24 ferrobasalt. *Proc. Lunar Planet. Sci. Conf.* **10**, 439-
783 478.
- 784 Hill E., Wood B. J. and Blundy J. D. (2000) The effect of Ca-Tschermaks component on
785 trace element partitioning between clinopyroxene and silicate melt. *Lithos* **53**, 203-
786 215.
- 787 Hollister L. S. and Gancarz A. J. (1971) Compositional sector-zoning in clinopyroxene from
788 the Narce area, Italy. *Am. Mineral.* **56**, 959-979.

789 Kahl M., Chakraborty S., Pompilio M. and Costa F. (2015) Constraints on the nature and
790 evolution of the magma plumbing system of Mt. Etna volcano (1991–2008) from a
791 combined thermodynamic and kinetic modelling of the compositional record of
792 minerals. *J. Petrol.* **56**, 2025-2068.

793 Kahl M., Viccaro M., Ubide T., Morgan D. J. and Dingwell D. B. (2017) A branched magma
794 feeder system during the 1669 eruption of Mt Etna: Evidence from a time-integrated
795 study of zoned olivine phenocryst populations. *J. Petrol.* **58**, 443-472.

796 Kent, A. J., Till, C. B. & Cooper, K. M. (2023) Start me up: The relationship between
797 volcanic eruption characteristics and eruption initiation mechanisms. *Volcanica* **6**,
798 161-172.

799 Kouchi A., Sugawara Y., Kashima K. and Sunagawa I. (1983) Laboratory growth of sector
800 zoned clinopyroxenes in the system $\text{CaMgSi}_2\text{O}_6\text{-CaTiAl}_2\text{O}_6$. *Contrib. Mineral. Petrol.*
801 **83**, 177-184.

802 Landi P., La Felice S., Petrelli M., Vezzoli L. M. and Principe C. (2019) Deciphering textural
803 and chemical zoning of k-feldspar megacrysts from mt. Amiata volcano (southern
804 tuscany, italy): Insights into the petrogenesis and abnormal crystal growth. *Lithos* **324**,
805 569-583.

806 Leung I. S. (1974) Sector-zoned titanaugites: Morphology, crystal chemistry, and growth.
807 *Am. Mineral.* **59**, 127-138.

808 Lofgren G. (1980) Experimental studies on the dynamic crystallization of silicate melts.
809 *Physics of Magmatic Processes*. Princeton Univ. Press 487-551
810 MacDonald A., Ubide T.,
811 Mollo S., Masotta M. and Pontesilli A. (2022) Trace element partitioning in zoned
812 clinopyroxene as a proxy for undercooling: Experimental constraints from
trachybasaltic magmas. *Geochim. Cosmochim. Acta* **336**, 249-268.

813 Magee R., Ubide T. and Kahl M. (2020) The lead-up to Mount Etna's most destructive
814 historic eruption (1669). Cryptic recharge recorded in clinopyroxene. *J. Petrol.* **61**,
815 egaa025.

816 Magee R., Ubide T. and Caulfield J. (2021) Days to weeks of syn-eruptive magma
817 interaction: High-resolution geochemistry of the 2002-03 branched eruption at Mount
818 Etna. *Earth Planet. Sci. Lett.* **565**, 116904.

819 Masotta M., Pontesilli A., Mollo S., Armienti P., Ubide T., Nazzari M. and Scarlato P. (2020)
820 The role of undercooling during clinopyroxene growth in trachybasaltic magmas:
821 Insights on magma decompression and cooling at Mt. Etna volcano. *Geochim.*
822 *Cosmochim. Acta* **268**, 258-276.

823 Métrich N., Allard P., Spilliaert N., Andronico D. and Burton M. (2004) 2001 flank eruption
824 of the alkali-and volatile-rich primitive basalt responsible for Mount Etna's evolution
825 in the last three decades. *Earth Planet. Sci. Lett.* **228**, 1-17.

826 Mollo S., Blundy J., Iezzi G., Scarlato P. and Langone A. (2013) The partitioning of trace
827 elements between clinopyroxene and trachybasaltic melt during rapid cooling and
828 crystal growth. *Contrib. Mineral. Petrol.* **166**, 1633-1654.

829 Mollo S., Giacomoni P. P., Coltorti M., Ferlito C., Iezzi G. and Scarlato P. (2015)
830 Reconstruction of magmatic variables governing recent etnean eruptions: Constraints
831 from mineral chemistry and P-T-fo₂-H₂O modeling. *Lithos* **212**, 311-320.

832 Mollo S. and Hammer J. (2017) Dynamic crystallization in magmas. *EMU Notes Mineral* **16**,
833 373-418.

834 Mollo S., Blundy J., Scarlato P., De Cristofaro S. P., Tecchiato V., Di Stefano F., Vetere F.,
835 Holtz F. and Bachmann O. (2018) An integrated PT-H₂O-lattice strain model to
836 quantify the role of clinopyroxene fractionation on REE+ Y and HFSE patterns of

837 mafic alkaline magmas: Application to eruptions at Mt. Etna. *Earth-Science Reviews*
838 **185**, 32-56.

839 Mollo S., Blundy J., Scarlato P., Vetere F., Holtz F., Bachmann O. and Gaeta M. (2020) A
840 review of the lattice strain and electrostatic effects on trace element partitioning
841 between clinopyroxene and melt: Applications to magmatic systems saturated with
842 tschermak-rich clinopyroxenes. *Earth Sci. Rev.* **210**, 103351.

843 Mollo S., Moschini P., Ubide T., MacDonald A., Vetere F., Nazzari M., Misiti V., Miyajima
844 M., Melai C., Di Genova D., Vona A., Di Fiore F., and Romano C. (2023) Kinetic
845 partitioning of trace cations between zoned clinopyroxene and a variably cooled-
846 decompressed alkali basalt: Thermodynamic considerations on lattice strain and
847 electrostatic energies of substitution. *Geochim. Cosmochim. Acta* **361**, 40–66.

848 Moschini P., Mollo S., Gaeta M., Fanara S., Nazzari M., Petrone C. M. and Scarlato P.
849 (2021) Parameterization of clinopyroxene growth kinetics via crystal size distribution
850 (csd) analysis: Insights into the temporal scales of magma dynamics at Mt. Etna
851 volcano. *Lithos* **396**, 106225.

852 Morimoto N. (1988) Nomenclature of Pyroxenes. *Min. and Petrol.* **39**, 59 – 76.

853 Mulas M., Cioni R., Andronico D. and Mundula F. (2016) The explosive activity of the 1669
854 Monti Rossi eruption at Mt. Etna (Italy). *J. Volcanol. Geotherm. Res.* **328**, 115-133.

855 Müller T., Dohmen R., Becker H., Ter Heege J. H. and Chakraborty S. (2013) Fe–Mg
856 interdiffusion rates in clinopyroxene: Experimental data and implications for Fe–Mg
857 exchange geothermometers. *Contrib. Mineral. Petrol.* **166**, 1563-1576.

858 Müntener O., Kelemen P. B. and Grove T. L. (2001) The role of H₂O during crystallization
859 of primitive arc magmas under uppermost mantle conditions and genesis of igneous
860 pyroxenites: An experimental study. *Contrib. Mineral. Petrol.* **141**, 643-658.

861 Nakamura Y. (1973) Origin of sector-zoning of igneous clinopyroxenes. *Am. Mineral.* **58**,
862 986-990.

863 Neave D. A., MacLennan J., Hartley M. E., Edmonds M. and Thordarson T. (2014) Crystal
864 storage and transfer in basaltic systems: The Skuggafjöll eruption, Iceland. *J. Petrol.*
865 **55**, 2311-2346.

866 Neave D. A. and Putirka K. D. (2017) A new clinopyroxene-liquid barometer, and
867 implications for magma storage pressures under icelandic rift zones. *Am. Mineral.*
868 **102**, 777-794.

869 Neave D. A., Bali E., Guðfinnsson G. H., Halldórsson S. A., Kahl M., Schmidt A.-S. and
870 Holtz F. (2019) Clinopyroxene–liquid equilibria and geothermobarometry in natural
871 and experimental tholeiites: The 2014–2015 Holuhraun eruption, Iceland. *J. Petrol.*
872 **60**, 1653-1680.

873 Onuma N., Higuchi H., Wakita H. and Nagasawa H. (1968) Trace element partition between
874 two pyroxenes and the host lava. *Earth Planet. Sci. Lett.* **5**, 47-51.

875 Paton C., Hellstrom J., Paul B., Woodhead J. and Hergt J. (2011) Iolite: Freeware for the
876 visualisation and processing of mass spectrometric data. *J. Anal. At. Spectrom.* **26**,
877 2508-2518.

878 Perinelli C., Mollo S., Gaeta M., De Cristofaro S. P., Palladino D. M., Armienti P., Scarlato
879 P. and Putirka K. D. (2016) An improved clinopyroxene-based hygrometer for etnean
880 magmas and implications for eruption triggering mechanisms. *Am. Mineral.* **101**,
881 2774-2777.

882 Petrus J., Chew D., Leybourne M. and Kamber B. (2017) A new approach to laser-ablation
883 inductively-coupled-plasma mass-spectrometry (la-icp-ms) using the flexible map
884 interrogation tool ‘monocle’. *Chem. Geol.* **463**, 76-93.

885 Pontesilli A., Masotta M., Nazzari M., Mollo S., Armienti P., Scarlato P. and Brenna M.
886 (2019) Crystallization kinetics of clinopyroxene and titanomagnetite growing from a
887 trachybasaltic melt: New insights from isothermal time-series experiments. *Chem.*
888 *Geol.* **510**, 113-129.

889 Pontesilli A., Brenna M., Ubide T., Mollo S., Masotta M., Caulfield J., Le Roux P., Nazzari
890 M., Scott J. and Scarlato P. (2021) Intraplate basalt alkalinity modulated by a
891 lithospheric mantle filter at the Dunedin volcano (New Zealand). *J. Petrol.* **62**,
892 egab062.

893 Putirka K. D. (2008) Thermometers and barometers for volcanic systems. *Rev. Mineral.*
894 *Geochem.* **69**, 61-120.

895 Ruth D. and Costa F. (2021) A petrological and conceptual model of mayon volcano
896 (philippines) as an example of an open-vent volcano. *Bull. Volcanol.* **83**, 62.

897 Sack, R.O. and Carmichael, I.S.E., (1984) $Fe^{2+} \rightleftharpoons Mg^{2+}$ and $TiAl_2 \rightleftharpoons MgSi_2$ exchange reactions
898 between clinopyroxenes and silicate melts. *Contrib. Mineral. Petrol.*, **85**, 103-115.

899 Shannon R. D. (1976) Revised effective ionic radii and systematic studies of interatomic
900 distances in halides and chalcogenides. *Acta Crystallogr.* **32**, 751-767.

901 Shea T. and Hammer J. E. (2013) Kinetics of cooling-and decompression-induced
902 crystallization in hydrous mafic-intermediate magmas. *J. Volcanol. Geotherm. Res.*
903 **260**, 127-145.

904 Shimizu N. (1981) Trace element incorporation into growing augite phenocryst. *Nature* **289**,
905 575-577.

906 Smith R. K. and Lofgren G. E. (1973) An analytical and experimental study of zoning in
907 plagioclase. *Lithos* **16** 153-168.

908 Streck M. J. (2008) Mineral textures and zoning as evidence for open system processes. *Rev.*
909 *Mineral. Geochem.* **69**, 595-622.

910 Tapu A., Ubide T. and Vasconcelos P. (2022) Plumbing system architecture of late-stage
911 hotspot volcanoes in eastern australia. *J. Petrol.* **63**, egac015.

912 Ubide T., McKenna C. A., Chew D. M. and Kamber B. S. (2015) High-resolution LA-ICP-
913 MS trace element mapping of igneous minerals: In search of magma histories. *Chem.*
914 *Geol.* **409**, 157-168.

915 Ubide T. and Kamber B. S. (2018) Volcanic crystals as time capsules of eruption history.
916 *Nature Commun.* **9**, 1-12.

917 Ubide T., Mollo S., Zhao J.-x., Nazzari M. and Scarlato P. (2019a) Sector-zoned
918 clinopyroxene as a recorder of magma history, eruption triggers, and ascent rates.
919 *Geochim. Cosmochim. Acta* **251**, 265-283.

920 Ubide T., Caulfield J., Brandt C., Bussweiler Y., Mollo S., Di Stefano F., Nazzari M. and
921 Scarlato P. (2019b) Deep magma storage revealed by multi-method elemental
922 mapping of clinopyroxene megacrysts at Stromboli volcano. *Front. Earth Sci.* **7**, 239.

923 Ubide T., Neave D. A., Petrelli M. and Longpré M.-A. (2021) Crystal archives of magmatic
924 processes. *Front. Earth Sci.*, 722. **9**, 749100.

925 Ubide T., Márquez Á., Ancochea E., Huertas M. J., Herrera R., Coello-Bravo J. J., Sanz-
926 Mangas D., Mulder J., MacDonald A. and Galindo I. (2023) Discrete magma
927 injections drive the 2021 La Palma eruption. *Sci. Adv.* **9**, eadg4813.

928 Van Orman J. A., Grove T. L. and Shimizu N. (2001) Rare earth element diffusion in
929 diopside: Influence of temperature, pressure, and ionic radius, and an elastic model
930 for diffusion in silicates. *Contrib. Mineral. Petrol.* **141**, 687-703.

931 Viccaro M., Barca D., Bohron W. A., D'Oriano C., Giuffrida M., Nicotra E. and Pitcher B.
932 W. (2016) Crystal residence times from trace element zoning in plagioclase reveal
933 changes in magma transfer dynamics at Mt. Etna during the last 400 years. *Lithos*
934 **248**, 309-323.

935 Wang Z.-C., Zhou M.-F., Li M. Y. H., Robinson P. T. and Harlov D. E. (2022) Kinetic
936 controls on Sc distribution in diopside and geochemical behavior of Sc in magmatic
937 systems. *Geochim. Cosmochim. Acta.* **325**, 316-332.

938 Wood B. J. and Blundy J. D. (2001) The effect of cation charge on crystal–melt partitioning
939 of trace elements. *Earth Planet. Sci. Lett.* **188**, 59-71.

940 Zhou, J.S., Wang, Q., Xing, C.M., Ma, L., Hao, L.L., Li, Q.W., Wang, Z.L. and Huang, T.Y.
941 (2021) Crystal growth of clinopyroxene in mafic alkaline magmas. *Earth Planet. Sci.*
942 *Lett.* **568**, 117005.

943
944
945
946

947 **Figure Captions**

948 Fig. 1: Schematic illustration of magmatic pathways at Mt. Etna, Italy (redrawn after Ubide
949 and Kamber, 2018) with eruptions studied in this work. Eccentric pathways are indicated in
950 blue and bypass the central conduit system, indicated in green. All summit eruptions are fed
951 by the vertically extended, complex central conduit plumbing system. Flank eruptions are
952 often fed by the central conduits but can also feed from eccentric pathways, offering a more
953 direct ascent pathway that may be conducive to high magma undercooling. Insert map shows
954 the location of Mt. Etna on the island of Sicily, Italy.

955 Fig. 2: LA-ICP-MS compositional maps of representative clinopyroxene crystals from the
956 1669, 1974 and 2002-03 eruptions at Mt. Etna, Italy. Crystal zones (core, mantle and rim) and
957 sectors (prism and hourglass) are marked for each crystal. White dashed lines on Cr maps
958 indicate crystal edges. All crystals presented here record mafic rejuvenation as indicated by
959 Cr enrichments coupled with depletions in high field strength elements (e.g., Zr and Ta) and

960 rare earth elements (e.g., Ce and Yb) (Ubide and Kamber, 2018). Data for the 1974
961 microphenocrysts are from Ubide et al. (2019b). Concentration scales are quantitative for
962 clinopyroxene and semi-quantitative for other phases included in the maps (see Methods).

963 Fig. 3: Major and minor cation contents (in atoms per formula unit; apfu) plotted against Mg#
964 ($\text{MgO}/(\text{MgO} + \text{FeO}_t) \times 100$ on molar basis) of sector-zoned mantles of clinopyroxene crystals
965 from the 1974 eccentric, 2002-03 eccentric and 1669 flank (central conduit) eruptions. Data
966 from 1974 and 2002-03 are from Ubide et al. (2019b). Light grey circles indicate
967 clinopyroxene literature data from GEOROC (<https://georoc.eu/>), obtained on 24/8/22 using
968 the following parameters: geological setting = complex: volcanic settings = Etna/Sicily:
969 mineral/component = augite/clinopyroxene: rock type = volcanic rock: type of material:
970 mineral and was further filtered to only include clinopyroxene from trachybasalts (Table S5).

971 Fig. 4: Comparison of tetrahedral aluminium ($^{\text{T}}\text{Al}$) in Cr-rich mantle zones of clinopyroxene
972 across different eruptions at Mt. Etna and crystal sizes as kernel density estimates. The
973 average $^{\text{T}}\text{Al}$ content for hourglass and prism sectors for each population is marked below the
974 plot, and highlights increasing enrichment in $^{\text{T}}\text{Al}$ in prism relative to hourglass sector with
975 decreasing crystal size.

976 Fig. 5: a) Sector enrichment of minor and trace elements in clinopyroxene, calculated as the
977 ratio between the concentration in prism sectors $\{h k 0\}$ to hourglass sectors $\{-1 1 1\}$, in Cr-
978 rich mantle zones. Values are plotted as a function of ionic potential, which is the ratio of the
979 charge of the cation (Z) and the square of the ionic radius (r^2), as proposed in Shimizu (1981)
980 and applied to Mt. Etna in Ubide et al. (2019b). Cation radii are from Shannon (1976) in IV-
981 fold (T site), VI-fold (M1 site) and VIII-fold (M2 site) coordinations. For Al, we only
982 consider the radius for IV-fold coordination (tetrahedral site). Plotted values represent

983 average sector enrichments for each eruption, and error bars represent one standard deviation.

984 b) Sector enrichment of the isovalent series of REE series occupying the M2 site.

985 Fig. 6: Sector enrichment of selected HFSE (Zr, Ta) and REE (Ce, Y) as a function of crystal
986 width. Uncertainties were propagated from $2 \times$ standard errors from extracted LA-ICP-MS
987 data. Sector enrichment increases with decreasing crystal width (increasing magma
988 undercooling).

989 Fig. 7: Undercooling (ΔT) calculated using clinopyroxene-melt REE partition coefficients
990 (MacDonald et al., 2022) from hourglass sectors of 1974 and 2002-03 clinopyroxene crystals,
991 and using the clinopyroxene-only major element model of Masotta et al., (2020). As per
992 previous figures, we only consider the Cr-rich mantle zones. The dashed line in the top plot
993 represents the experimentally determined upper limit of ΔT for sector-zoned clinopyroxene
994 (Kouchi et al., 1983; Masotta et al., 2020). Undercooling modelled from natural crystals
995 agree with sector zoning developing at $\Delta T < 45^\circ\text{C}$, with microphenocrysts from the 1974
996 eccentric eruption returning slightly higher undercooling than larger crystals from the
997 eccentric and central conduit eruptions.

998 Fig. 8: Relationship between calculated ΔT and concentration of large ion lithophile elements
999 (LILE; Li), transition metals (Cr) and high field strength elements (HFSE; Zr and Ta) in
1000 hourglass sectors of our clinopyroxene crystals. Simple linear regression yields variable
1001 coefficients of determination (R^2) across the range of examined elements. Only the HFSE
1002 define a clear positive correlation with ΔT , as expected from their dependence on charge
1003 balancing substitutions (Ubide et al., 2019a; MacDonald et al., 2022). Error bars represent 2
1004 \times standard error from data extracted from LA ICP-MS compositional maps.

1005 Fig. 9: a) Total Alkali Silica (TAS) diagram comparing matrix (microcrystalline groundmass)
1006 compositions from the 2021 La Palma eruption, (ocean island basalt system, Canary Islands),

1007 the Roman era Pizzo activity at Stromboli volcano (Italy, arc), and the 1974 and 2002-03
1008 eruptions at Mt. Etna (Italy). Data from the 2021 La Palma eruption are from Ubide et al.
1009 (2023), data from Stromboli are from Ubide et al. (2019b) and data from the Mt. Etna
1010 eruptions are from Magee et al. (2020, 2021).

1011 b) Kernel density estimates (KDE) of tetrahedral aluminium (^TAl) from hourglass and prism
1012 sectors of Cr-rich zones associated with eruption triggering mafic rejuvenation from
1013 clinopyroxene megacrysts from Stromboli Ubide et al. (2019b), La Palma (Ubide et al., 2023)
1014 and Etna (this study; full details of this plot are reported in Fig. 4). Average hourglass and
1015 prism ^TAl contents are indicated by empty and filled triangles, respectively. Difference
1016 between ^TAl content of hourglass and prism sectors are indicated by the bars below each plot.
1017 Values are reported rounded to 2 decimal places. Melt composition modulates absolute Al
1018 concentrations in clinopyroxene, yet Al enrichment between sectors is independent of melt
1019 composition and modulated by magma dynamics, increasing with ΔT from megacrysts to
1020 phenocrysts to microphenocrysts across eruptions and magmatic compositions.

1021

1022

1023

1024